Numerical simulation of PM2.5 dispersion originated from vehicular traffic in urban environments: Situational validation of proposed biomonitoring method

Václav Mikulec
vaclav.mikulec@seznam.cz

Czech University of Life Sciences Prague

Research Article

Keywords: $PM_{2.5}$, CFD, ANSYS Fluent, Discrete Phase Model, k–ω SST, Biomonitoring, Urban vegetation

Posted Date: March 12th, 2026

DOI: https://doi.org/10.21203/rs.3.rs-7742066/v1

Additional Declarations: No competing interests reported.

Title: Numerical simulation of PM2.5 dispersion originated from vehicular traffic in urban environments: Situational validation of proposed biomonitoring method

Author: Václav Mikulec

Affiliation: Faculty of Environmental Sciences, Czech University of Life Sciences Prague, Kamýcká 129, Praha – Suchdol, 165 00, Czech Republic

Abstract:

Vehicular PM2.5 emissions pose a major urban air-quality challenge, particularly in dense street canyons. We developed a high-resolution CFD model (≈14.8 million cells) in ANSYS Fluent to simulate dispersion and deposition in a geo-referenced 3D domain representing a Prague roadway. The k–ω SST turbulence model, coupled with the Discrete Phase Model and energy equation, resolved airflow, heat–mass exchange, and particle trajectories. Vegetation was parameterized as an isotropic porous medium with calibrated Darcy–Forchheimer coefficients to capture canopy resistance and interception. Transient particle injections mimicking emissions from Euro 5 vehicles were applied under urban breeze and traffic-wake turbulence. Results identified hotspots linked to braking near signals and recirculation zones, with ≈65% of PM2.5 advected downstream and the rest deposited or intercepted, particularly by dense grasses. Model predictions of heavy-metal deposition agreed with biomonitoring using *Calamagrostis epigejos*. This integrated CFD–biomonitoring framework supports design of vegetation and traffic-flow interventions to improve air quality.

Keywords: $PM_{2.5}$; CFD; ANSYS Fluent; Discrete Phase Model; k–ω SST; Biomonitoring; Urban vegetation

1 Introduction

1.1 Motivation and Research Rationale

The principal driving force behind the present investigation was a deep dive into the potential of agile biomonitoring specifically, the collection of expansive grasses growing in close proximity to traffic corridors—to quantify pollutant loads originating from road transport. Our work builds on the methodology detailed in *Using Expansive Grasses for Monitoring Heavy-Metal Pollution in the Vicinity of Roads* (Vachová et al., 2017). Repeated applications of that protocol inevitably raised a pivotal question:

How do local aerodynamics shape the final deposition of traffic-related pollutants on the surface of the sampled vegetation?

Although the contemporary literature boasts an impressive array of studies on $PM_{2.5}$ dispersion, their goals and scales often diverge from ours (Gromke & Ruck, 2012; Tominaga & Stathopoulos, 2011; M. Zhou et al., 2022). Typical urban-scale assessments focus on how a source affects a predefined area or how land-use planning and architectural design can mitigate adverse micro-climatic phenomena (Britter & Hanna, 2003; Gromke & Ruck, 2007; F. Li et al., 2022; Z. Li et al., 2021). For practical reasons, these models usually span large domains and incorporate complex building geometries, yet they seldom resolve vortex structures at the meter scale—let alone particle capture on individual leaves.

Meanwhile, steady advances in computing power—still dutifully tracking Gordon Moore's prophetic curve (Moore, 2006)—now allow remarkably detailed numerical simulations on desktop workstations, computations that not long ago required an entire super-computing facility. Harnessing this progress, the present study adopts an experimental design mindset: we construct a finely resolved, geo-referenced spatial domain at full scale, which serves as the foundation for simulating $PM_{2.5}$ dispersion from a moving vehicular source into its immediate surroundings. In doing so, we aim to contribute an integrated view of fine-particulate behavior in built environments and, on that basis, refine the vegetation-sampling protocol for biomonitoring.

1.2 Literature Background

Early work by Gromke and Ruck laid the groundwork for incorporating vegetation into computational fluid dynamics (CFD) studies of urban pollution. They introduced a porous-media approach to represent trees and shrubs as momentum sinks, demonstrating that vegetation can significantly alter flow structures within street canyons. Through combined wind-tunnel experiments and CFD simulations, Research by (Gromke & Ruck, 2007) showed that both the arrangement of trees and their crown density critically influence pollutant recirculation zones: in some configurations, dense tree canopies can trap pollutants at street level, while in others they enhance ventilation and pollutant removal.

Building on this foundation, recent research has moved toward district-scale modelling by coupling real traffic emissions data with both Reynolds-averaged Navier–Stokes (RANS) and large-eddy simulation (LES) frameworks. Simulations by (M. Zhou et al., 2022) integrated time-varying traffic flows into their CFD models, validating simulated $PM_{2.5}$ concentrations against in-situ measurements across entire urban districts. This approach captures both the spatial heterogeneity and temporal fluctuations of particulate dispersion, offering a more comprehensive picture of urban air quality dynamics.

Complementing these numerical methods, biomonitoring using expansive grasses has proven an effective empirical tool for assessing particulate deposition. Methodic of (Vachová et al., 2017) established a robust protocol based on nitric-acid extraction and atomic absorption spectroscopy to quantify heavy metals and $PM_{2.5}$ collected on *Calamagrostis epigejos* leaf surfaces. They determined an optimal extraction procedure and sampling timeframe and found that short-term rainfall had minimal impact on measured deposition, ensuring consistency across variable weather conditions (Mahbub et al., 2010). Moreover, this grass-based approach is both more economical and flexible than stationary monitoring stations, requiring minimal equipment and maintenance while providing broader spatial coverage. Finally, the study demonstrated that extracted solutions can be stored indefinitely without loss of analyte integrity, enabling further analysis such as speciation or source apportionment—well beyond the field campaign period.

1.3 Ecotoxicology Aspects

From an ecotoxicological perspective, “heavy metals” encompass all metallic elements that pose a potential environmental burden—among them cadmium, chromium, copper, nickel, lead and zinc (*Handbook on the Toxicology of Metals*, 2007). These elements are emitted as fine particulate matter ($PM_{2.5}$) during brake-pad and disc wear, fuel combustion and engine component abrasion in road traffic (Thorpe & Harrison, 2008). The result is a complex dust mixture that often also contains polycyclic aromatic hydrocarbons (PAHs), persistent organic pollutants and unburned fuel residues (Fan et al., 2019).

Owing to their extremely small size and high specific surface area, $PM_{2.5}$ particles readily adsorb a variety of organic and inorganic compounds. Thus, heavy metals in the atmosphere rarely occur in isolation but rather in combination with other toxic substances, which can interact synergistically to amplify adverse effects on both human health and ecosystems. Once airborne, these particles are transported by wind, with their travel distance and spatial distribution governed by meteorological conditions (e.g. wind speed, temperature gradients) and terrain features. Deposition occurs via both dry settling onto soils and vegetation and wet deposition through precipitation events, which can further leach bound contaminants into soils and water bodies (Alloway, 2013; Luch, 2009).

After reaching soils and aquatic environments, heavy metals can persist for long periods due to strong affinities for organic matter and fine sediment fractions. Their propensity for bioaccumulation and biomagnification leads to increasing concentrations up the food chain—from plankton and benthic invertebrates through fish predators to terrestrial predators and ultimately humans (Nordberg, 2007).

In humans, these metals bind to proteins and enzymes, disrupting essential metabolic pathways. While copper, zinc and nickel serve as essential trace elements at low concentrations, excess exposure induces toxic effects such as renal, hepatic and respiratory damage. Lead and cadmium accumulation is particularly pernicious, often causing irreversible neurological impairments. In aquatic ecosystems, elevated metal and co-pollutant levels impair fish reproduction, osmoregulation and immune and endocrine functions; similar effects in invertebrate prey species threaten biodiversity and destabilize entire food webs (Linhart, 2014; World Health Organization, 2006; Zhang et al., 2017).

2 Methods

2.1 Biomonitoring

2.1.1 Species Choice

We selected *Calamagrostis epigejos* as the primary bioindicator species due to its dense above-ground canopy, which reaches peak biomass in mid-summer, and its demonstrated capacity to retain fine particulate matter on leaf surfaces. This expansive grass is also resilient to drought and temperature extremes, ensuring reliable field performance even adjacent to busy roadways (Sæbø et al., 2012). As a secondary candidate, *Lolium perenne* was considered because of its rapid regrowth following mowing. However, its lower long-term pollutant accumulation and susceptibility to overshadowing by taller species make it less suitable for our study area; nevertheless, it remains a viable option for biomonitoring in landscapes subject to frequent mowing (Vachová et al., 2017).

2.1.2 Field Campaign

The field campaign was conducted along Evropská Street in Prague—a primary artery connecting the city to Václav Havel Airport—on 30 October 2024. Nine sampling zones were identified to capture variations in particulate exposure under differing aerodynamic conditions. At each zone, we harvested above-ground portions of *C. epigejos*, aiming for a dry biomass of approximately 6 g per sample (the mean dry mass recorded was 5.95 g). Harvested material was immediately placed into 1 L sampling bottles avoiding contamination and stored chilled until laboratory processing.

2.1.3 Laboratory Workflow

In the laboratory, each grass sample underwent nitric-acid extraction following the protocol of (Vachová et al., 2017), with minor adaptations. Specifically, 100 mL of a 2 M HNO_3 solution was added to each sample in a 1 L extraction flask. Samples were manually shaken for 300 s at a rate of roughly 100 oscillations per minute to desorb particulate-bound metals into solution. After extraction, the mixture was filtered to remove plant debris, and approximately 30 mL of filtrate was reserved for analysis. Final quantification of cadmium (Cd), chromium (Cr), copper (Cu), nickel (Ni), lead (Pb), and zinc (Zn) in the extracts were performed by a third-party laboratory using atomic absorption spectrometry (AAS).

2.2. CFD Workflow

2.2.1 Urban Geometry & Experimental Design

To investigate the coupled effects of urban heat islands, street-tunnel ventilation, and local urban breezes on particulate dispersion, a detailed 3D model of a representative street canyon was developed and preprocessed for CFD simulation (Oke et al., 2017; Rizwan et al., 2008).

A 3D georeferenced model covering an area of approximately 180 m × 50 m horizontally and 30 m vertically was constructed in Autodesk InfraWorks and Inventor. In this workflow, real vegetation elements (trees, shrubs) were substituted with simplified solid volumes to facilitate reliable mesh generation. Subsequently the geometry was imported into ANSYS SpaceClaim and Fusion for domain preprocessing. This included patching small gaps, stitching adjacent surfaces, detaching separate bodies, and assigning logical names to all inlet, outlet, wall, and symmetrical boundaries in preparation for meshing and boundary-condition specifications.

2.2.2 Boundary Conditions and Flow Forcing

A conventional inlet–outlet arrangement was employed to drive airflow primarily along the street axis, corresponding to prevailing traffic directions. The northern face of the domain was designated as an ambient inlet to impose an urban-breeze profile originating from a nearby natural reserve, while all remaining lateral and top surfaces were set as outflow boundaries. Road-axis inlets were represented as 8 m-wide rectangular patches on either side of the carriageway. Their velocities were tuned to replicate the mean wind speed encountered at the boundary between roadway and roadside—approximately 1.5 m above the pavement, where a passing passenger vehicle traveling at 70 km/h generates about 8 m/s (≈ 30 km/h) of air movement (Cai et al., 2020; Eskridge & Hunt, 1979; Shi et al., 2020). At these primary traffic inlets, we prescribed a turbulent intensity of 15 % and a turbulent-viscosity ratio of 10 to mimic the strong shear and mixing in a vehicle's wake. For the smaller roadside inlets, a lower velocity of 1 m/s with 5 % turbulent intensity and the same viscosity ratio was used to capture the gentler recirculating flow beside stationary vehicles (Tab. 1). Here, turbulent intensity, *I*, quantifies the root-mean-square of velocity fluctuations as a percentage of the mean velocity:

$$I = \frac{sqrt\left(\left(\frac{2}{3}\right)*k\right)}{U_{mean}} \qquad (1.1)$$

while the turbulent-viscosity ratio, $\frac{\nu_t}{\nu}$, sets the initial eddy viscosity relative to the molecular viscosity, ensuring realistic onset of turbulence without excessive numerical diffusion (Versteeg & Malalasekera, 2007).

Tab. 1 - Boundary-condition settings for each enclosure zone

Enclosure Zone	BC type	DPM interaction	Velocity [m/s]	Turbulent intensity [%]	Turbulent viscosity ratio [-]
OUTLET	Outflow	Escape	-	-	-
RS	Velocity inlet	Escape	1	5	10
LS	Outflow	Escape	-	-	-
TOP	Outflow	Escape	-	-	-
INLET	Outflow	Escape	-	-	-
inlet_out	Velocity inlet	Escape	8	15	10
inlet_in	Outflow	Escape	-	-	-
outlet_out	Outflow	Escape	-	-	-
outlet_in	Velocity inlet	Escape	8	15	10

2.2.3 Meshing Strategy

All meshing was performed directly in ANSYS Fluent after exporting fully watertight geometry from SpaceClaim, following the recommended transfer workflow to eliminate pre-mesh incompatibilities. Using Fluent's meshing tools, we generated a hybrid grid of unstructured tetrahedral cells in the bulk flow regions and prismatic (inflation) layers adjacent to all solid boundaries. The element sizes ranged from a minimum edge length of 25 mm in refined zones to a maximum of 694 mm in far-field regions. Five inflation layers were applied normal to each wall to accurately resolve boundary-layer gradients. The resulting mesh comprised 14.8 million cells, with over 90 % exhibiting skewness values between 0.4 and 0.7 after multiple refinements, comfortably within recommended limits for accurate flow and particle tracking.

2.2.4 Vegetation Representation

To capture the aerodynamic effect of urban vegetation on airflow and particulate transport, each of the 26 vegetation volumes was treated as an isotropic porous medium defined by a porosity ϕ and by two calibrated resistance coefficients: the viscous coefficient C_0 and the inertial coefficient C_1 (Tab. 2).

The momentum-sink term added to the i-th momentum equation is given by the Darcy–Forchheimer law (Nield & Bejan, 2017):

$$S_{\{m,i\}} = -\left(\mu \cdot C_0 \cdot u_i + ½ \cdot \rho \cdot C_1 \cdot |u| \cdot u_i \right) \tag{1.2}$$

- μ = fluid's dynamic viscosity
- ρ = fluid density
- u_i = i-th component of the local velocity vector u
- |u| = magnitude of u

In this expression, the term $\mu \cdot C_0 \cdot u_i$ represents the linear (Darcy) drag dominating at low Reynolds numbers, and the term $\left(\frac{1}{2}\right) \cdot \rho \cdot C_1 \cdot |u| \cdot u_i$ represents the quadratic (Forchheimer) drag that becomes significant at higher velocities (Nield & Bejan, 2017).

The Darcy–Forchheimer formulation combines a linear drag term, which dominates in low-velocity, creeping flows through dense vegetation, with a quadratic drag term that becomes significant under high-speed gusts around canopy edges, thereby providing accurate pressure-loss predictions across a wide range of flow regimes. By representing vegetation as homogeneous porous blocks rather than resolving every individual leaf and branch, it dramatically reduces mesh complexity and solver run times, making largescale urban CFD simulations far more computationally efficient. Moreover, the model's resistance coefficients can be directly calibrated through simple wind-tunnel experiments; by fitting measured pressure drops (Δp) against mean flow velocities (u) to the equation $\Delta p = \mu \cdot C_0 \cdot u + ½ \cdot \rho \cdot C_1 \cdot u^2$, one obtains site- and species-specific values for C_0 and C_1, ensuring both physical fidelity and adaptability to diverse vegetation types (Koch et al., 2019).

By applying the calibrated values of C_0 (in m^{-2}) and C_1 (in m^{-1}) uniformly to each porous zone (Tab. 2), the model reproduces both the damping of mean flow by dense vegetation and the enhanced turbulence generated by stronger gusts through tree canopies—achieving realistic canopy-scale flow modifications without the meshing and runtime costs of explicit foliage representation.

The Darcy–Forchheimer drag formulation was applied to capture both viscous and inertial pressure losses through the canopy volumes, leveraging the advantages of this approach as documented by (Koch et al., 2019).

Tab. 2 - Porous-media properties for vegetation zones

Porous zone	Viscous resistance [m^2]	C_0	C_1	Porosity	Count [-]
Bushes	2111000	300	1.5	0.77	5
Foliage_small	211100	100	1.3	0.86	15
Foliage_big	21110	50	1	0.92	6

2.2.5 Discrete Phase Model (DPM) Configuration

Particulate injections were implemented via ANSYS Fluent's Discrete Phase Model. The road surface served as the emission source, with injection parameters calibrated to represent the passage of approximately four Euro 5 standard vehicles in both directions during the simulation period. Emission angles (Tab. 3) were set based on typical plume orientations from vehicle exhaust systems and drivetrain (Qin et al., 2024; Tominaga & Stathopoulos, 2013).

Tab. 3 - Injection-source parameters for discrete-phase model

Injections	X [m/s]	Y [m/s]	Z [m/s]	tO [s]	tX [s]	T [K]	Flow [kg/s]	d [m]	m [ug]	Count [-]
Injection_in	-20	12	-5	0	2.2	320	2.13×10^{-8}	2.50E-06	0.0234	453,390
Injection_out	20	12	5	0	2.2	320	2.13×10^{-8}	2.50E-06	0.0234	453,390

2.2.6 Initial Conditions

In our simulations, the temperature field was initialized to reflect measured variations in surface and near-surface air temperatures across the study domain (Tab. 4). Zones adjacent to paved surfaces—such as "Road_in," "Road_out," and the gravel strip—were assigned higher initial temperatures (309 K and 305 K, respectively) to capture heat stored during daytime traffic and solar insolation. Vegetated belts and tree trunks were set to slightly lower values (ranging from 295 K under the canopy to 302 K in mid-road grass), reflecting evapotranspirative cooling and shading effects (Oke, 2006; Oke et al., 2017; Sini et al., 1996). Inlet boundaries carrying ambient breeze and traffic-induced flow were assigned temperatures matching their adjacent zones to avoid artificial thermal jumps at the domain entry points.

For the Discrete Phase Model, "trap" interactions were applied on walls, vegetation, and ground surfaces where particle deposition is expected. In Fluent, a trap condition means a particle must physically encounter the boundary face at a nonzero normal velocity and at the first computational cell adjacent to that face, which corresponds to $y^+ \approx 0$, before it is removed from the discrete phase. This ensures that only particles that truly intersect the surface layer—rather than those passing within the viscous sublayer—are counted as deposited, faithfully mimicking the fluid-mechanical requirement for particulate interception and adhesion in real canopies and on solid surfaces (Matsson, 2024).

Tab. 4 - Zone-specific thermal and DPM boundary conditions

Zone	Temperature [K]	DPM interaction	BC type	Count [-]
Trunks	295	Reflect	Wall	23
Grass_far (grassy belt behind gravel road)	296	Trap	Wall	1
Bushes	296	Trap	Internal	5
LS_inlet (inlet simulating Urban Breeze)	296	Escape	Velocity inlet	1
Foliage_big (grown trees)	297	Trap	Internal	6
Foliage_small (mid road trees)	299	Trap	Internal	15
Grass_main (dominant grass zone)	299	Trap	Wall	1
Grass_mid (mid road grass belt)	302	Trap	Wall	1
Outlet_in (inlet towards city center)	302	Reflect	Velocity inlet	1
Gravel (gravel road)	305	Trap	Wall	1
Inlet_out (inlet out of city center)	307	Reflect	Velocity inlet	1
Metallic (metallic surfaces)	308	Reflect	Wall	8
Road_in (roadway towards city center)	309	Reflect	Wall	1
Road_out (roadway out of city center)	309	Reflect	Wall	1

2.2.7 K-Ω SST TURBULENCE MODEL

The k-ω Shear Stress Transport (SST) model, developed by Florian Menter (F. R. Menter, 1994, 2009), employs a hybrid concept that combines the strengths of two two-equation turbulence formulations to enhance predictive capability in complex flows. Near solid boundaries, the model adopts the k-ω formulation, renowned for its superior accuracy in capturing boundary-layer behavior without the need for additional damping functions. In the free stream and wake regions, it gradually transitions to the k-ε formulation, which offers greater robustness and numerical stability away from walls. This blending is governed by a smooth blending function that activates the appropriate turbulence closure in each region, ensuring a seamless switch between formulations and avoiding abrupt changes in model constants (F. R. Menter, 2009; Shih et al., 1995; Wilcox, 2006).

2.2.7.1 TURBULENT KINETIC ENERGY (K) TRANSPORT EQUATION (F. R. MENTER, 1994)

$$\frac{\partial(\rho \cdot k)}{\partial t} + \frac{\partial(\rho \cdot u_j \cdot k)}{\partial x_j} = P_k - \beta_* \cdot \rho \cdot k \cdot \omega + \frac{\partial}{\partial x_j\left[(\mu + \sigma_k \cdot \mu_t) \cdot \frac{\partial k}{\partial x_j}\right]} \quad (1.3)$$

- ρ = fluid density
- u_j = velocity component in j direction
- P_k = turbulence production term
- β_* = model constant
- ω = specific dissipation rate
- μ = molecular viscosity
- μ_t = turbulent (eddy) viscosity
- σ_k = turbulent Prandtl number for *k*

2.2.7.2 SPECIFIC DISSIPATION RATE (Ω) TRANSPORT EQUATION (F. R. MENTER, 1994)

$$\frac{\partial(\rho \cdot \omega)}{\partial t} + \frac{\partial(\rho \cdot u_j \cdot \omega)}{\partial x_j} =$$

$$\alpha \cdot \left(\frac{\omega}{k}\right) \cdot P_k - \beta \cdot \rho \cdot \omega_2 + \frac{\partial}{\partial x_j\left[(\mu + \sigma_\omega \cdot \mu_t) \cdot \frac{\partial \omega}{\partial x_j}\right]} + 2 \cdot (1 - F_1) \cdot \left(\rho \cdot \frac{\sigma_{\{\omega_2\}}}{\omega}\right) \cdot \frac{\partial k}{\partial x_j} \cdot \frac{\partial \omega}{\partial x_j} \quad (1.4)$$

- α, β, σ_ω, $\sigma_{\{\omega_2\}}$ = model constants
- F_1 = blending function (→1 near walls, →0 in free stream)
- The last term is the cross-diffusion correction.

2.2.7.3 *Eddy viscosity definition with shear-stress limiter (Wilcox, 2006)*

$$\mu_t = \frac{\rho \cdot a_1 \cdot k}{\max(\, a_1 \cdot \omega, S \cdot F_2)}$$

$$where\;\; S = \sqrt{2 \cdot S_{\{ij\}} \cdot S_{\{ij\}}},$$

$$S_{\{ij\}} = ½ \cdot \left(\frac{\partial u_i}{\partial x_j} + \frac{\partial u_j}{\partial x_i}\right) \tag{1.5}$$

- a_1 = model constant
- S = invariant measure of strain rate:
- F_2 = second blending function (similar form to F_1)

2.2.7.4 *Blending functions (Pope, 2000)*

$$F_1 = tanh\left(\left[min\left(max\left(\frac{\sqrt{k}}{\beta^* \omega y}, \frac{500\nu}{y^2\omega}\right), \frac{4\sigma_{\{\omega_2\}}k}{CD_{k\omega}y^2}\right)\right]^4\right)$$

$$F_2 = tanh\left(\left[max\left(\frac{2\sqrt{k}}{\beta^* \omega y}, \frac{500\nu}{y^2\omega}\right)\right]^2\right)$$

$$CD_{k\omega} = max\left(\frac{2\rho\frac{\sigma_{\{\omega_2\}}\left(\frac{1}{\omega}\right)\partial k}{\partial x_j \partial \omega}}{\partial x_j}, 10^{-10}\right) \tag{1.6}$$

By taking the maximum of the computed cross-diffusion term and a small positive floor, the model avoids numerical singularities and ensures that the blending functions remain bounded and differentiable even in regions where either k or ω gradients vanish, preventing division by zero (F. Menter & Egorov, 2005; F. R. Menter, 2009; Pope, 2000).

2.2.8 One-Way Coupled Discrete Phase Model (DPM)

For dilute particle concentrations where particles do not affect the continuous phase, each particle's trajectory is governed by (Matsson, 2024):

2.2.8.1 Particle momentum equation

$$d\frac{u_p}{dt} = \left(\frac{1}{\tau_p}\right) \cdot \left(u - u_p\right) + g \cdot \frac{\rho_p - \rho}{\rho_p} + F_{other}$$

$$with\ \tau_p = \rho_p \cdot \frac{d_p^2}{(18 \cdot \mu)} \tag{1.7}$$

- u_p = particle velocity vector
- u = local fluid velocity vector
- τ_p = particle relaxation time
- ρ_p = particle density
- d_p = particle diameter
- g = gravity vector
- F_{other} = additional forces (e.g., thermophoretic, Brownian if included)

2.2.8.2 Particle position update

$$d\frac{x_p}{dt} = u_p \tag{1.8}$$

- x_p = particle position vector

The detailed architecture of the k-ω SST model includes transport equations for the turbulent kinetic energy (k) and the specific dissipation rate (ω). The model modifies the standard k-ω equations by introducing a limiter on the turbulent shear stress to prevent excessive turbulent production in adverse pressure gradients, and by re-deriving certain closure coefficients to improve physical consistency. The blending function F_1 controls the mixing of model constants, such that $F_1 \approx 1$ in the inner region (applying nearly pure k-ω) and $F_1 \approx 0$ in the outer region (applying nearly pure k-ε). This approach retains the k-ω model's accuracy in predicting near-wall gradients while benefiting from the k-ε model's well-established behavior in free-stream flows (F. R. Menter, 1994; Pope, 2000).

Compared to the standard k-ε model, k-ω SST offers significantly improved resolution of flow separation and recirculation zones behind buildings and vegetation canopies—critical features in urban street-canyon simulations. At the same time, it remains far less computationally intensive than large-eddy simulation (LES), making it a pragmatic choice for high-resolution district-scale studies where capturing detailed turbulence structures is necessary but full LES would be prohibitively expensive (Sagaut, 2006).

In our ANSYS Fluent case, several add-on modules further enhance the k-ω SST model's performance. The curvature correction accounts for the stabilizing or destabilizing influence of streamline curvature on turbulence production, improving vortex prediction around curved surfaces (Spalart & Shur, 1997). The corner-flow correction refines turbulence behavior in regions with orthogonal walls, such as building intersections (Matsson, 2024). Finally, the Kato–Launder modification improves numerical stability in high-strain regions by adapting the eddy-viscosity formulation (Wilcox, 2006). Together, these enhancements yield a robust and accurate turbulence closure suited to the complex aerodynamic interactions present in urban environments (Matsson, 2024).

2.2.9 Numerical Setup

The numerical simulations employed an unsteady Discrete Phase Model (DPM) to track particle trajectories over time. A total of 210 time steps, each of 0.15 s, were used to ensure that the majority of injected particles either deposited on surfaces or exited the domain. The time-step size was chosen to maintain a Courant number of approximately 1.2, balancing temporal resolution with solver stability (Wesseling, 2009).

An initial simulation run of roughly 20 s revealed that a significant fraction of particles remained airborne, necessitating an extension of the simulation period to fully capture their transport and fate. To address occasional convergence issues in regions of high flow strain—particularly near sharp corners and within recirculation zones—slight under-relaxation factors were applied to the momentum and turbulence equations. These adjustments improved numerical stability without unduly prolonging run times (Versteeg & Malalasekera, 2007).

All simulations were conducted on a desktop workstation equipped with a 32-core AMD Threadripper CPU, demonstrating that high-fidelity urban CFD studies remain feasible on non-cluster hardware. Parallel processing across 12 cores reduced wall-clock time substantially, making this approach accessible to research groups without access to large-scale supercomputing facilities.

Given the 14.8 million–cell hybrid tetra/prism mesh, we employed a full-multigrid (FMG) initialization to accelerate convergence of the steady-state flow field before enabling the unsteady DPM tracking. Without FMG, convergence was markedly slower: standard single-level multigrid runs required more iterations to reach acceptable residual levels and often exhibited spurious oscillations in the velocity and turbulence fields (Ferziger & Perić, 2002). With FMG, continuity, momentum, turbulent kinetic energy, and specific-dissipation-rate residuals all dropped below 10^{-1} within the first 100 multigrid cycles, providing a robust starting point for the transient particulate simulation. We also observed that pausing the unsteady simulation and then continuing it led to a small rebound in residuals—particularly for the turbulence equations—before they re-settled to their pre-pause levels within a few dozen time steps. This transient increase likely reflects the re-initialization of the solver's internal under-relaxation and multigrid buffers upon restart, but did not materially affect the overall particle-tracking results.

3 Results

The following subsections present key findings from our coupled CFD–biomonitoring study. Firstly, details of the transient flow fields (Fig. 1) and particle-tracking snapshots (Fig. 2) are shown, illustrating the development of recirculation zones, pollutant hotspots and residence-time distributions. Full details on the computational setup—including the mesh, ANSYS case files, solver settings, and complete time-step exports with variable views—are provided in the Supplementary Materials, along with the raw particle-tracking outputs and processed deposition data. All data and scripts used in this study are also available in the attached archive.

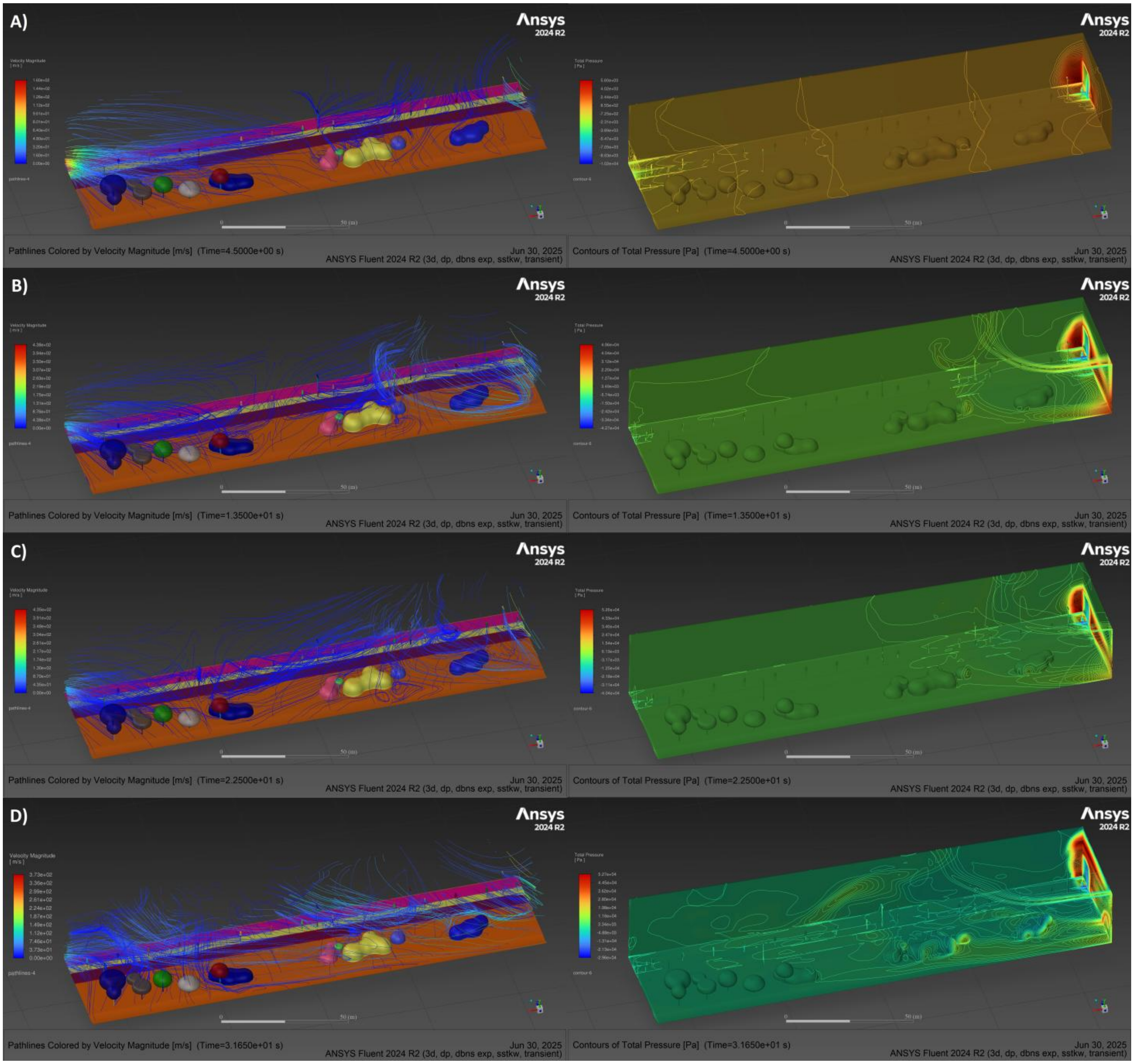

Fig. 1 - Snapshots of instantaneous flow and pressure fields in the street-canyon model[1]

[1] Streamlines colored by velocity magnitude (left) and total-pressure contours (right) at four-time instants after start of injection: **A)** 4.5 s **B)** 13.5 s **C)** 22.5 s **D)** 31.65 s. Each panel shows the development of the near-ground recirculation zones, wake structures behind vegetation volumes, and the evolution of the high-pressure front at the upstream inlet.

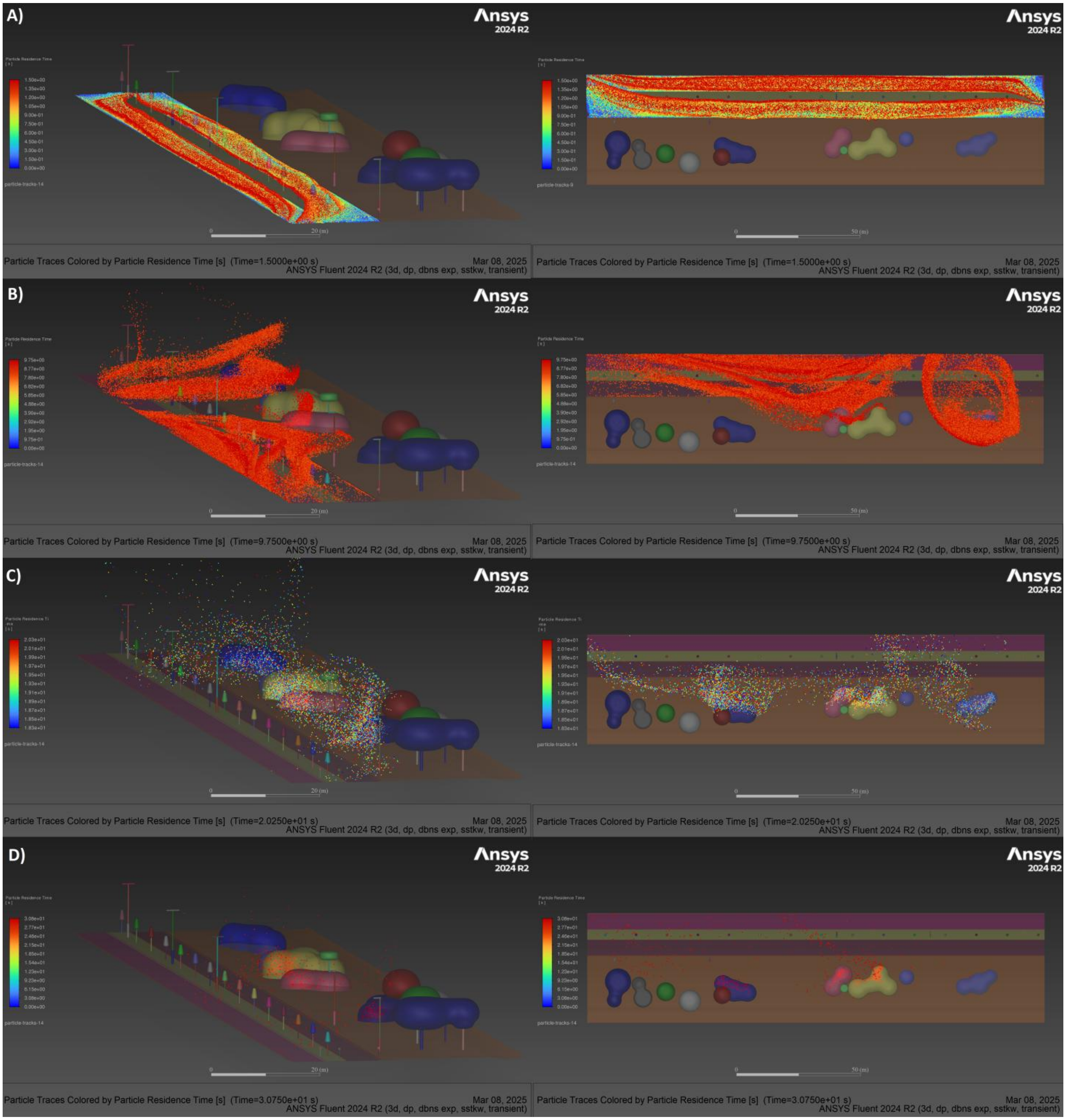

Fig. 2 - Snapshots of $PM_{2.5}$ particle residence-time distributions in the street-canyon model[2]

[2] Particle traces colored by residence time (s) at four-time instants after injection start: **A)** 1.50 s **B)** 9.75 s **C)** 20.25 s **D)** 30.75 s. Left sub-panels show an oblique 3D view of the canyon with vegetation volumes; right sub-panels show a longitudinal cross-section. The progression illustrates initial rapid transport along the canyon floor, subsequent buildup in recirculation zones around trees and bushes, and eventual dispersion and deposition near walls and vegetation.

For each metal, the nine samples were ranked from highest to lowest concentration and assigned value from nine (highest concentration) down to one (lowest concentration). The values awarded for each metal were then summed across all metals to give a total weight gain for each sample (Fig. 3). The CFD simulations and biomonitoring data both indicate that the eastern sector of the study domain experiences higher $PM_{2.5}$ concentrations than other areas. This elevated pollution level is attributable to repeated braking emissions at the nearby traffic lights and reduced near-surface airflow in the leeward recirculation zone. Biomonitoring samples 2, 1, and 3—collected in this eastern sector—showed the highest heavy-metal concentration, confirming the model's prediction of pollutant hotspots, contradicting this observation, sample 5 came as the least polluted from the biomonitoring, but simulation clearly showed this zone as one of the main hotspots for $PM_{2.5}$ flow (Fig. 2: B, C).

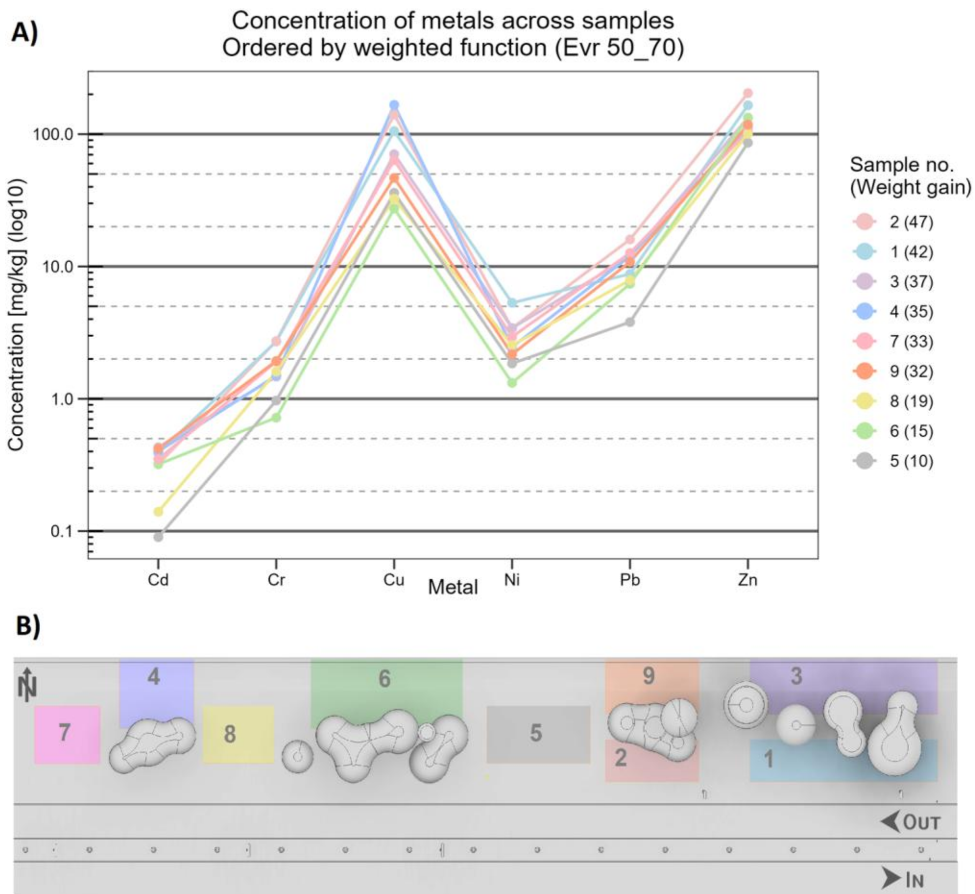

Fig. 3 - Heavy-metal concentration profiles and sampling-site layout[3]

[3] **(A)** Concentrations of Cd, Cr, Cu, Ni, Pb and Zn ($mg\ kg^{-1}$, log_{10} scale) in *Calamagrostis epigejos* samples (n = 9), ordered by weighted deposition index (Evr 50_70). **(B)** Plan view of the street-canyon test section showing the spatial extents of each sampling zone. Colored rectangles correspond to the sample numbers in (A); round wireframes depict the clustered foliage volumes around each biomonitoring zone. The roadway footprint is shown in gray beneath.

Across the seven depositional zones from research conducted in 2023 (Fig. 4), median Cd and Cr concentrations in *C. epigejos* and *L. perenne* were highest at the Lipská highway sites (Lip 90 and Lip 130), reflecting greater wear-and-tear emissions under high-speed traffic; notably, Lip 130 exhibited the widest interquartile ranges and most extreme outliers for Cu and Zn, suggesting episodic spikes—likely from braking or acceleration events. By contrast, the low-speed, heavily vegetated Vizerka (Viz) and Veleslavín (Vel 50) zones showed both lower medians and tighter spreads for all metals, indicating more consistent, background-level deposition. The two Evropská recirculation zones (Evr 70, Evr 50) fell between these extremes, with Pb and Ni medians elevated relative to Viz/Vel 50 but below Lipská levels, underscoring the role of canyon vortex trapping.

Species comparisons reveal that *C. epigejos* consistently accumulated higher median loads of Cu, Pb and Zn than *L. perenne*, and also displayed larger variability—particularly at Lip 90/130—demonstrating its superior interception surface and sensitivity to localized hotspots. For Ni, both grasses showed similar medians, but again *C. epigejos's* broader whiskers and outliers highlight its stronger uptake under peak emissions. Cd and Cr levels remained low across species and areas, yet *C. epigejos* captured the highest single Cd and Cr outlier at Evr 50, suggesting that even low-traffic recirculation can concentrate these metals under certain conditions. Overall, the boxplots confirm that traffic intensity and flow dynamics are primary drivers of metal deposition, and that *C. epigejos* serves as a more responsive biomonitoring specie than *L. perenne*.

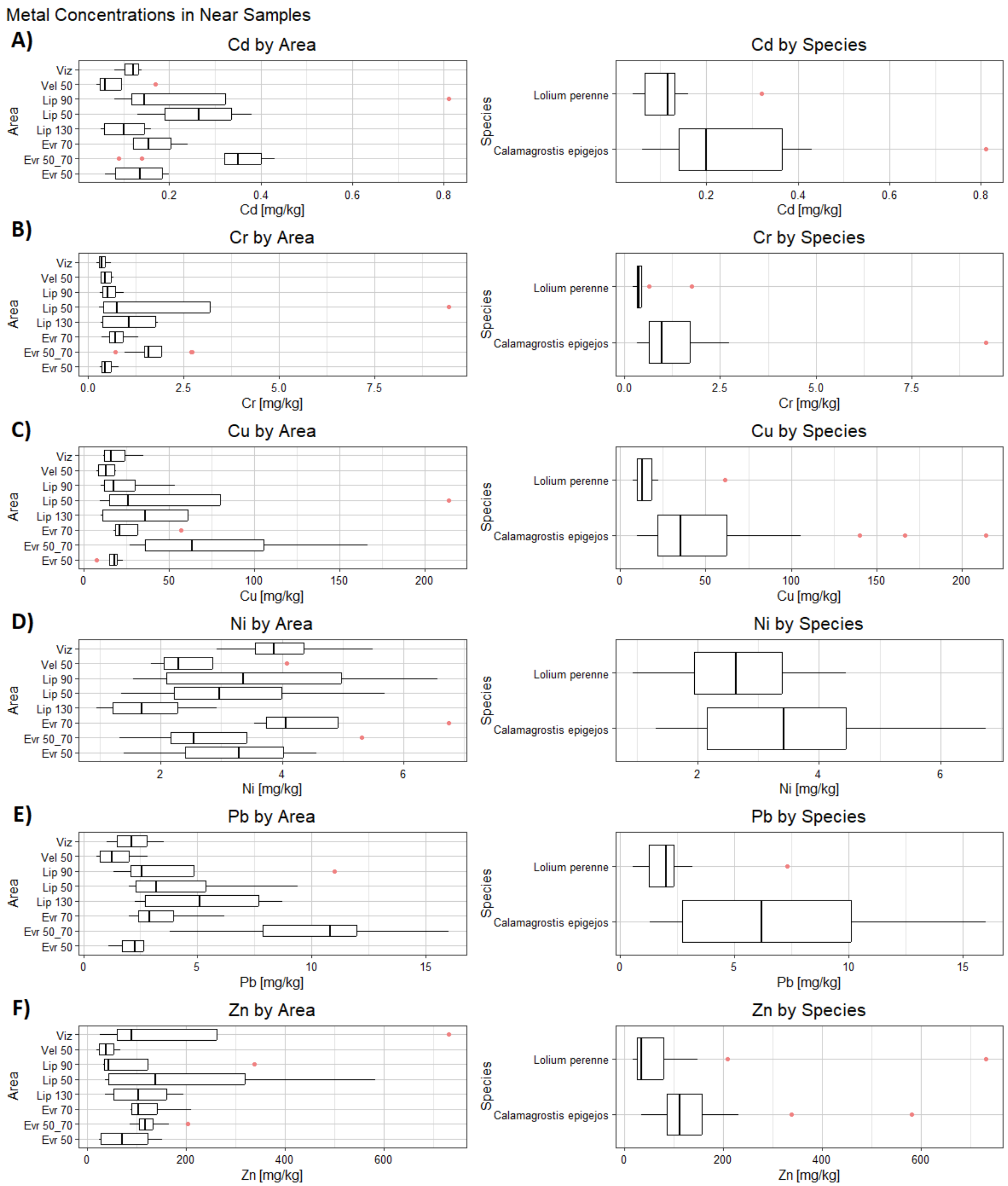

Fig. 4 - Box-and-whisker distributions of heavy metal concentrations by sampling area and species[4]

[4] Sampling areas: Viz = Vizerka unpaved road; Vel 50 = Veleslavín crossing (50 km/h); Lip 90/50/130 = Lipská highway at 90, 50 and 130 km/h; Evr 70/50 = Evropská street at 70 and 50 km/h. All samples except Evr 50_70 were collected and analyzed in 2023. Left sub-panels plot concentrations by area; right sub-panels compare deposition between researched species. (Map of sampling zones available in [supplementary material])

In contrast, the western sector exhibited pronounced vertical lift of particulate matter, driven by the more open local geometry. Here, the absence of tightly enclosed canyon walls allowed $PM_{2.5}$ to ascend more readily into the mid-canopy region, reducing ground-level deposition rates. This finding underscores, how slight variations in urban form can redirect particle transport pathways.

In fact, two-thirds of all particles ultimately exited the domain in the direction of traffic flow, indicating substantial potential for long-range $PM_{2.5}$ advection by vehicular flow potentially creating above average polluted bottlenecks upstream. The remaining one-third of particles were either trapped within the domain, including those escaping through the top outlet, which represents a source of wider dispersion—or deposited on surfaces (Fig. 5).

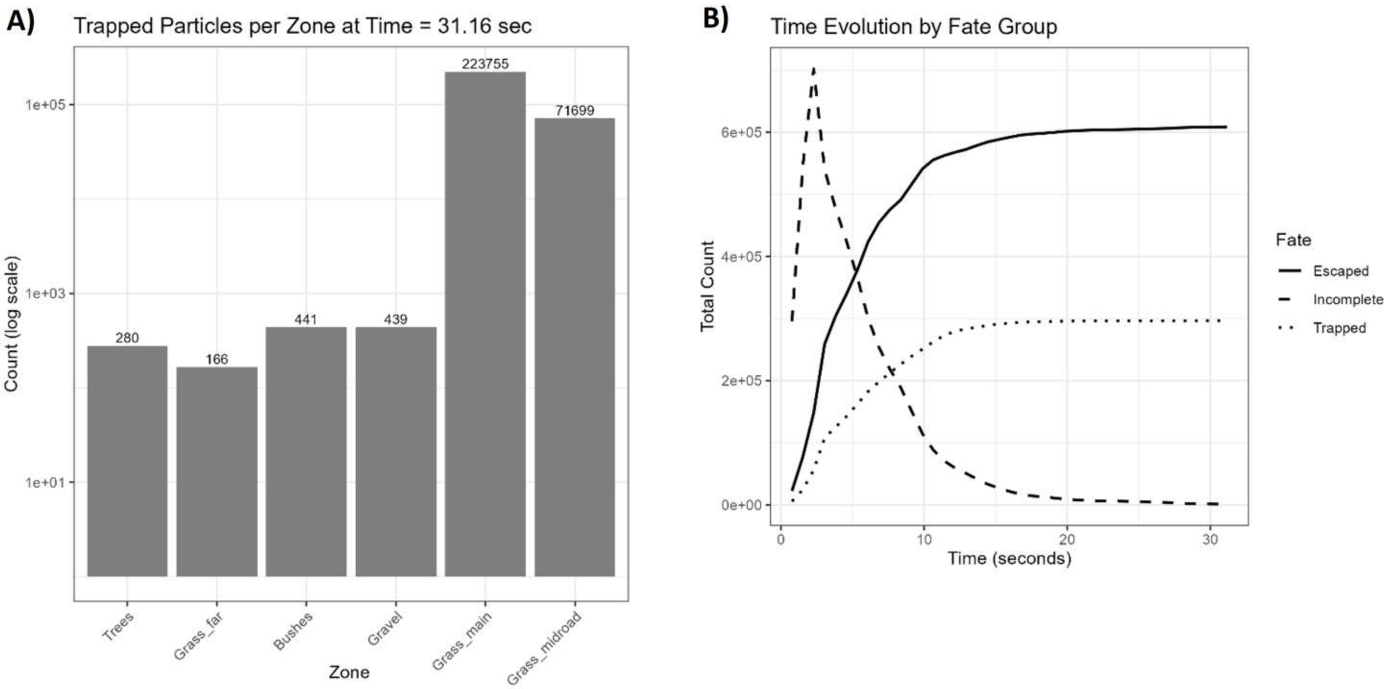

Fig. 5 – Trapped particle distribution and temporal evolution[5]

After 32 s of simulation, approximately 1,200 particles were still airborne within porous bush volumes (Fig. 2,Fig. 5 – Trapped particle distribution and temporal evolution Fig. 5). These particles can be considered effectively trapped by the vegetation, highlighting the role of dense shrubs and grasses as particulate sinks. In contrast, canopy-scale trees—while imposing significant aerodynamic resistance—captured fewer particles per unit volume, suggesting that lower, denser vegetation provides more surface area for $PM_{2.5}$ interception.

Finally, analysis of particle kinematics revealed that $PM_{2.5}$, due to its small size and low inertia, loses most of its initial velocity almost immediately upon emission. Consequently, its transport is governed primarily by the local wind field generated by traffic

[5] **A)** Depicts final trapped particle distribution. By 31 s, the main grass belt (Grass_main) has intercepted the vast majority of particles ($\approx 2.2 \times 10^5$), followed by the mid-road grass ($\approx 7.2 \times 10^4$). All other zones—trees, distant grass, bushes and gravel—trap fewer than 500 particles each, highlighting the superior trapping efficiency of dense grass cover. **B)** Follows particle fate evolution through simulation. The incomplete-fate curve peaks early (≈2.5 s), reflecting particles still airborne, then falls to zero as they either escape or deposit. The escaped population rises sharply and plateaus around 6×10^5, indicating most particles exit the canyon, while the trapped curve climbs steadily to $\approx 3 \times 10^5$, demonstrating progressive deposition over time.

flow and ambient weather conditions, rather than by inertial carry-off. This behavior reinforces the importance of accurately modeling urban airflow patterns when predicting fine-particle dispersion and deposition in street canyons.

4 DISCUSSION

Several factors introduce uncertainty into the present study's findings. First, vegetation sampling took place late in the vegetative season, when *Calamagrostis epigejos* biomass and its capacity for particulate accumulation may have been reduced (Y. Zhou et al., 2022). Moreover, variability in municipal mowing schedules—ranging from twice weekly in recreational areas to as few as three to eight cuts per year along main roads—means that available biomass and deposition patterns can differ substantially between zones. Finally, analytical blank exhibited unexpected lead contamination, which could marginally skew deposition estimates for that metal, though overall trends across multiple elements remain clear.

On the numerical side, our CFD approach relies on several simplifying assumptions. Emissions were treated as spatially and temporally uniform, whereas real traffic flows exhibit stochastic variability in vehicle speed, acceleration, and fleet composition (Hudda et al., 2013). Vegetation was represented as isotropic porous objects rather than fully resolved foliage geometries, which may underestimate localized flow distortion and particle interception at canopy edges.

Preprocessing of urban geometry also introduced complications. During automatic stitching and duplicate-body removal in the CAD workflow, several adjacent sampling-zone volumes were erroneously merged into a single "grass_main" body. In addition: It is possible to obtain a digital terrain model directly from Autodesk InfraWorks via map-based selection; however, the exported surfaces in STEP or STL formats are often highly tessellated, making each preprocessing step—patching, stitching, and duplicate removal—exceptionally RAM-intensive and time-consuming before meshing can proceed (Pađen et al., 2022).

A systematic mesh-independence study could demonstrate the potential to reduce the total cell count below 14.8 million while preserving key flow and deposition features, thereby accelerating future simulations without sacrificing accuracy. To strengthen confidence in these results, further validation is required. In-situ measurements of wind-speed profiles, detailed traffic counts (including braking events), and high-resolution temperature distributions across the domain would provide richer boundary conditions and independent benchmarks for the CFD model.

Despite these limitations, the combined CFD and biomonitoring methodology proved highly complementary. High-resolution flow and particle-tracking simulations identified pollutant-hotspot zones that matched elevated heavy-metal loads in grass samples, while empirical deposition patterns guided the interpretation of complex recirculation features in the eastern canyon. This integrated approach offers both spatially detailed predictions and ground-truth verification.

5 CONCLUSION

In comparing our findings with the broader literature, several parallels emerge. Work of (Gromke & Ruck, 2007) showed that dense tree canopies can both trap pollutants in leeward recirculation zones and enhance ventilation under certain arrangements—mirroring our eastern-sector hotspots and western-sector lofting. In their research (Y. Zhou et al., 2022), using district-scale LES coupled to real traffic data, reported pronounced spatial heterogeneity and transient peaks linked to braking events, lending support to our local-scale hotspot identification. Wind-tunnel work by (Fellini et al., 2022) demonstrated that street trees alter concentration fields without a clear trend in net ventilation efficiency, consistent with our observation that low, dense grasses—not sparse trunks—serve as the dominant $PM_{2.5}$ sinks. Finally, (Britter & Hanna, 2003) report that, under neutral stratification in narrow street canyons, approximately 60–80 % of vehicle-emitted pollutants ventilate out over the roof level, with only 20–40 % depositing or remaining trapped within the canyon. Also (Gromke & Ruck, 2007), in wind-tunnel experiments on an idealized, tree-free canyon, measured surface deposition of about 30 % of particulate emissions—implying an escape fraction close to 70 %. Research by (Sini et al., 1996), using two-dimensional physical modelling with a line-source tracer, found that roughly 65 % of simulated exhaust pollutants were ejected from the canyon, closely matching our ~66 % downstream exit ratio.

Overall, the study demonstrates that desktop-scale, high-resolution CFD—when paired with an agile grass-based biomonitoring protocol—effectively characterizes fine-particulate dispersion in urban street canyons. The CFD model effectively identified pollutant hotspots driven by flow recirculation and traffic emissions, which were largely confirmed by heavy-metal accumulation patterns in grass samples—especially in leeward zones and near braking points. While denser low vegetation like *C. epigejos* proved to be more effective PM sinks than trees, structural differences in urban geometry significantly influenced particle dispersion and deposition. Overall, the integration of simulation and biomonitoring offers a cost-effective, scalable tool for targeting air quality interventions in cities.

6 REFERENCES

6.1 SUPPLEMENTARY MATERIALS & DATA

Supplementary materials and data available from 10.5281/zenodo.15855764

6.2 BIBLIOGRAPHY

Alloway, B. J. (Ed.). (2013). *Heavy metals in soils: Trace metals and metalloids in soils and their bioavailability* (3rd ed). Springer.

Britter, R. E., & Hanna, S. R. (2003). FLOW ANDDISPERSION INURBANAREAS. *Annual Review of Fluid Mechanics*, *35*(1), 469–496. https://doi.org/10.1146/annurev.fluid.35.101101.161147

Cai, C., Ming, T., Fang, W., De Richter, R., & Peng, C. (2020). The effect of turbulence induced by different kinds of moving vehicles in street canyons. *Sustainable Cities and Society*, *54*, 102015. https://doi.org/10.1016/j.scs.2020.102015

Eskridge, R. E., & Hunt, J. C. R. (1979). Highway Modeling. Part I: Prediction of Velocity and Turbulence Fields in the Wake of Vehicles. *Journal of Applied Meteorology*, *18*(4), 387–400. https://doi.org/10.1175/1520-0450(1979)018<0387:HMPIPO>2.0.CO;2

Fan, X., Chen, Z., Liang, L., & Qiu, G. (2019). Atmospheric PM2.5-Bound Polycyclic Aromatic Hydrocarbons (PAHs) in Guiyang City, Southwest China: Concentration, Seasonal Variation, Sources and Health Risk Assessment. *Archives of Environmental Contamination and Toxicology*, *76*(1), 102–113. https://doi.org/10.1007/s00244-018-0563-5

Fellini, S., Marro, M., Del Ponte, A. V., Barulli, M., Soulhac, L., Ridolfi, L., & Salizzoni, P. (2022). High resolution wind-tunnel investigation about the effect of street trees on pollutant concentration and street canyon ventilation. *Building and Environment*, *226*, 109763. https://doi.org/10.1016/j.buildenv.2022.109763

Ferziger, J. H., & Perić, M. (2002). *Computational methods for fluid dynamics* (3rd, rev. ed ed.). Springer.

Gromke, C., & Ruck, B. (2007). Influence of trees on the dispersion of pollutants in an urban street canyon—Experimental investigation of the flow and concentration field. *Atmospheric Environment*, *41*(16), 3287–3302. https://doi.org/10.1016/j.atmosenv.2006.12.043

Gromke, C., & Ruck, B. (2012). Pollutant Concentrations in Street Canyons of Different Aspect Ratio with Avenues of Trees for Various Wind Directions. *Boundary-Layer Meteorology*, *144*(1), 41–64. https://doi.org/10.1007/s10546-012-9703-z

Handbook on the Toxicology of Metals. (2007). Elsevier. https://doi.org/10.1016/b978-0-12-369413-3.x5052-6

Hudda, N., Fruin, S., Delfino, R. J., & Sioutas, C. (2013). Efficient determination of vehicle emission factors by fuel use category using on-road measurements: Downward trends on Los Angeles freight corridor I-710. *Atmospheric Chemistry and Physics*, *13*(1), 347–357. https://doi.org/10.5194/acp-13-347-2013

Koch, K., Samson, R., & Denys, S. (2019). Aerodynamic characterisation of green wall vegetation based on plant morphology: An experimental and computational fluid dynamics approach. *Biosystems Engineering*, *178*, 34–51. https://doi.org/10.1016/j.biosystemseng.2018.10.019

Li, F., Rubinato, M., Zhou, T., Li, J., & Chen, C. (2022). Numerical simulation of the influence of building-tree arrangements on wind velocity and PM2.5 dispersion in urban communities. *Scientific Reports*, *12*(1), 16378. https://doi.org/10.1038/s41598-022-20455-6

Li, Z., Ming, T., Shi, T., Zhang, H., Wen, C.-Y., Lu, X., Dong, X., Wu, Y., De Richter, R., Li, W., & Peng, C. (2021). Review on pollutant dispersion in urban areas-part B: Local mitigation strategies, optimization framework, and evaluation theory. *Building and Environment*, *198*, 107890. https://doi.org/10.1016/j.buildenv.2021.107890

Linhart, I. (2014). *Toxikologie: Interakce škodlivých látek s živými organismy, jejich mechanismy, projevy a důsledky* (2., upr. a rozš. vyd). Vysoká škola chemicko-technologická v Praze.

Luch, A. (2009). *Molecular, clinical, and environmental toxicology*. Birkhäuser.

Mahbub, P., Ayoko, G. A., Goonetilleke, A., Egodawatta, P., & Kokot, S. (2010). Impacts of Traffic and Rainfall Characteristics on Heavy Metals Build-up and Wash-off from Urban Roads. *Environmental Science & Technology*, *44*(23), 8904–8910. https://doi.org/10.1021/es1012565

Matsson, J. E. (2024). *An introduction to Ansys Fluent 2024*. SDC Publications.

Menter, F., & Egorov, Y. (2005, January 10). A Scale Adaptive Simulation Model using Two-Equation Models. *43rd AIAA Aerospace Sciences Meeting and Exhibit*. 43rd AIAA Aerospace Sciences Meeting and Exhibit, Reno, Nevada. https://doi.org/10.2514/6.2005-1095

Menter, F. R. (1994). Two-equation eddy-viscosity turbulence models for engineering applications. *AIAA Journal*, *32*(8), 1598–1605. https://doi.org/10.2514/3.12149

Menter, F. R. (2009). Review of the shear-stress transport turbulence model experience from an industrial perspective. *International Journal of Computational Fluid Dynamics*, *23*(4), 305–316. https://doi.org/10.1080/10618560902773387

Moore, G. E. (2006). Cramming more components onto integrated circuits, Reprinted from Electronics, volume 38, number 8, April 19, 1965, pp.114 ff. *IEEE Solid-State Circuits Society Newsletter*, *11*(3), 33–35. https://doi.org/10.1109/N-SSC.2006.4785860

Nield, D. A., & Bejan, A. (2017). *Convection in Porous Media*. Springer International Publishing. https://doi.org/10.1007/978-3-319-49562-0

Nordberg, G. (Ed.). (2007). *Handbook on the toxicology of metals* (3rd ed). Academic Press.

Oke, T. R. (2006). *Boundary layer climates* (2nd ed). Routledge.

Oke, T. R., Mills, G., Christen, A., & Voogt, J. A. (2017). *Urban Climates* (1st ed.). Cambridge University Press. https://doi.org/10.1017/9781139016476

Pađen, I., García-Sánchez, C., & Ledoux, H. (2022). Towards automatic reconstruction of 3D city models tailored for urban flow simulations. *Frontiers in Built Environment*, *8*. https://doi.org/10.3389/fbuil.2022.899332

Pope, S. B. (2000). *Turbulent flows*. Cambridge University Press.

Qin, P., Ricci, A., & Blocken, B. (2024). Modeling traffic pollutants in a street canyon by CFD: Idealized line sources versus multiple realistic car sources. *Science of The Total Environment*, *955*, 177099. https://doi.org/10.1016/j.scitotenv.2024.177099

Rizwan, A. M., Dennis, L. Y. C., & Liu, C. (2008). A review on the generation, determination and mitigation of Urban Heat Island. *Journal of Environmental Sciences*, *20*(1), 120–128. https://doi.org/10.1016/S1001-0742(08)60019-4

Sæbø, A., Popek, R., Nawrot, B., Hanslin, H. M., Gawronska, H., & Gawronski, S. W. (2012). Plant species differences in particulate matter accumulation on leaf surfaces. *Science of The Total Environment*, *427–428*, 347–354. https://doi.org/10.1016/j.scitotenv.2012.03.084

Sagaut, P. (2006). *Large eddy simulation for incompressible flows: An introduction* (3rd ed). Springer-Verlag.

Shi, X., Sun, D. (Jian), Zhang, Y., Xiong, J., & Zhao, Z. (2020). Modeling Emission Flow Pattern of a Single Cruising Vehicle on Urban Streets with CFD Simulation and Wind Tunnel Validation. *International Journal of Environmental Research and Public Health*, *17*(12), 4557. https://doi.org/10.3390/ijerph17124557

Shih, T.-H., Liou, W. W., Shabbir, A., Yang, Z., & Zhu, J. (1995). A new k-ϵ eddy viscosity model for high reynolds number turbulent flows. *Computers & Fluids*, *24*(3), 227–238. https://doi.org/10.1016/0045-7930(94)00032-T

Sini, J.-F., Anquetin, S., & Mestayer, P. G. (1996). Pollutant dispersion and thermal effects in urban street canyons. *Atmospheric Environment*, *30*(15), 2659–2677. https://doi.org/10.1016/1352-2310(95)00321-5

Spalart, P. R., & Shur, M. (1997). On the sensitization of turbulence models to rotation and curvature. *Aerospace Science and Technology*, *1*(5), 297–302. https://doi.org/10.1016/s1270-9638(97)90051-1

Thorpe, A., & Harrison, R. M. (2008). Sources and properties of non-exhaust particulate matter from road traffic: A review. *Science of The Total Environment*, *400*(1–3), 270–282. https://doi.org/10.1016/j.scitotenv.2008.06.007

Tominaga, Y., & Stathopoulos, T. (2011). CFD modeling of pollution dispersion in a street canyon: Comparison between LES and RANS. *Journal of Wind Engineering and Industrial Aerodynamics*, *99*(4), 340–348. https://doi.org/10.1016/j.jweia.2010.12.005

Tominaga, Y., & Stathopoulos, T. (2013). CFD simulation of near-field pollutant dispersion in the urban environment: A review of current modeling techniques. *Atmospheric Environment*, *79*, 716–730. https://doi.org/10.1016/j.atmosenv.2013.07.028

Vachová, P., Vach, M., & Najnarová, E. (2017). Using expansive grasses for monitoring heavy metal pollution in the vicinity of roads. *Environmental Pollution*, *229*, 94–101. https://doi.org/10.1016/j.envpol.2017.05.069

Versteeg, H. K., & Malalasekera, W. (2007). *An introduction to computational fluid dynamics: The finite volume method* (2nd ed). Pearson Education Ltd.

Wesseling, P. (2009). *Principles of computational fluid dynamics* (1st soft cover print). Springer.

Wilcox, D. C. (2006). *Turbulence modeling for CFD* (3rd ed). DCW Industries.

World Health Organization (Ed.). (2006). *Air quality guidelines: Global update 2005: particulate matter, ozone, nitrogen dioxide, and sulfur dioxide*. World Health Organization.

Zhang, Q., Jiang, X., Tong, D., Davis, S. J., Zhao, H., Geng, G., Feng, T., Zheng, B., Lu, Z., Streets, D. G., Ni, R., Brauer, M., Van Donkelaar, A., Martin, R. V., Huo, H., Liu, Z., Pan, D., Kan, H., Yan, Y., … Guan, D. (2017). Transboundary health impacts of transported global air pollution and international trade. *Nature*, *543*(7647), 705–709. https://doi.org/10.1038/nature21712

Zhou, M., Hu, T., Jiang, G., Zhang, W., Wang, D., & Rao, P. (2022). Numerical Simulations of Air Flow and Traffic–Related Air Pollution Distribution in a Real Urban Area. *Energies*, *15*(3), 840. https://doi.org/10.3390/en15030840

Zhou, Y., Chen, C., Lu, T., Zhang, J., & Chen, J. (2022). Season impacts on estimating plant's particulate retention: Field experiments and meta-analysis. *Chemosphere*, *288*, 132570. https://doi.org/10.1016/j.chemosphere.2021.132570